

## Article

# Enhanced Adsorption of Methyl Orange by Mongolian Montmorillonite after Aluminum Pillaring

Jiajun Chen <sup>1</sup>, Jianzun Lu <sup>1</sup>, Lingcheng Su <sup>1,\*</sup>, Huada Ruan <sup>1</sup>, Yijia Zhao <sup>1</sup>, Chiuhong Lee <sup>1</sup>, Zongwei Cai <sup>2</sup>, Zhihui Wu <sup>1</sup> and Yanan Jiang <sup>3,\*</sup>

<sup>1</sup> Environmental Science Program, Division of Science and Technology, United International College, Beijing Normal University–Hong Kong Baptist University, Zhuhai 519085, China; gzchenjiajun@163.com (J.C.); jianzunlu@uic.edu.cn (J.L.); hruan@uic.edu.cn (H.R.); yijiazhao@uic.edu.cn (Y.Z.); chiuhonglee@uic.edu.cn (C.L.); carwu@uic.edu.cn (Z.W.)

<sup>2</sup> Department of Chemistry, Faculty of Science, Hong Kong Baptist University, Hong Kong, China; zwcai@hkbu.edu.hk

<sup>3</sup> National Observation and Research Station of Coastal Ecological Environments in Macao, Macao Environmental Research Institute, Macau University of Science and Technology, Macao 999078, China

\* Correspondence: sulingcheng@163.com (L.S.); ynjia@must.edu.mo (Y.J.)

**Abstract:** This article studies the enhancement of methyl orange (MO) adsorption by Mongolian montmorillonite (MMt) modified by the intercalation of the Keggin Al<sub>13</sub> complex, followed by calcination during the pillaring process. The properties of MMt, Al-intercalated MMt (P-MMt), and Al-pillared MMt (P-MMt-C) were determined using X-ray diffraction (XRD), thermogravimetric analysis (TGA), surface-area analysis, and a field emission scanning electron microscope (FE-SEM). The MO adsorption by modified MMt was subsequently evaluated. The XRD basal distance (*d*<sub>001</sub>) and the specific surface area (SSA) increased after the modification of MMt. The TGA results revealed that P-MMt and P-MMt-C had better thermal stability than MMt. The Al-pillared MMt obtained after calcination (e.g., P-MMt-C400) showed a larger basal distance and surface area than that without pillaring. The MO adsorption process of P-MMt-C400 was supposed to be dominated by chemisorption and heterogeneous multilayer adsorption, according to the kinetic and isotherm studies. The maximum adsorption capacity of P-MMt-C400 is 6.23 mg/g. The MO adsorption ability of Al-pillared MMt was contributed by the Keggin Al<sub>13</sub> complex attracting MO and the increase in the surface area of macro-, meso- and micro-pores (>1.2 nm). The Al-pillared MMt in this study could be applied as an adsorbent in a water purification system to remove MO or other dye elements.

**Keywords:** adsorption; Al pillaring; calcination; methyl orange; montmorillonite



**Citation:** Chen, J.; Lu, J.; Su, L.; Ruan, H.; Zhao, Y.; Lee, C.; Cai, Z.; Wu, Z.; Jiang, Y. Enhanced Adsorption of Methyl Orange by Mongolian Montmorillonite after Aluminum Pillaring. *Appl. Sci.* **2022**, *12*, 3182. <https://doi.org/10.3390/app12063182>

Academic Editor: Juan García Rodríguez

Received: 7 February 2022

Accepted: 18 March 2022

Published: 21 March 2022

**Publisher's Note:** MDPI stays neutral with regard to jurisdictional claims in published maps and institutional affiliations.



**Copyright:** © 2022 by the authors. Licensee MDPI, Basel, Switzerland. This article is an open access article distributed under the terms and conditions of the Creative Commons Attribution (CC BY) license (<https://creativecommons.org/licenses/by/4.0/>).

## 1. Introduction

Dyes are useful chemicals for coloring products in order to increase their beauty and value. They are widely used in many products, such as textiles, leather, rubber, plastic, ceramic and paper [1]. Methyl orange (MO) is an acidic anionic mono-azo dye, and is commonly used in textiles, laboratory experiments, and other different commercial products [2]. Exposure to MO can cause health problems such as skin irritation, respiratory diseases and vomiting [3,4]. In addition, its degradation byproducts may increase the risk of cancers in different organs [5,6]. Various purification methods—including coagulation, flocculation, membrane filtration, oxidation, adsorption and biological treatment—are applied to remove the dye in wastewater [7]. Among those methods, adsorption is one of the most effective and economic methods to remove dyes in water and wastewater [8].

As natural adsorbents, clay minerals have been commonly applied to water purification due to their relatively large surface area, high cation exchange capacity, porosity, physical and chemical stability, and better swelling properties [9,10]. Due to the isomorphous substitution of Si<sup>4+</sup> by Al<sup>3+</sup> in the tetrahedral layer, or the similar substitution of Al<sup>3+</sup>

by  $Mg^{2+}$ ,  $Mn^{2+}$  and other cations with lower charges in the octahedral layer, MMt contains a permanent negative layer charge and variable charges at the surface [11]. As a result,  $Na^+$ ,  $K^+$ ,  $Ca^{2+}$  and other exchangeable cations can be attracted to the MMt interlayer and surface sites in order to balance the layer charges [9,12–14]. Therefore, MMt can remove cationic organic compounds, such as organic dyes, antibiotics, and other polar organics by electrostatic interaction [9,15–17].

Due to the hydrophilic property and negative charge of MMt, MMt is poor at adsorbing MO, which is an organic anionic compound. In order to enhance the adsorption ability of montmorillonite (MMt) towards MO, some modification methods are applied [18]. Pillaring is one of the common modification methods to enhance the surface and structural properties of MMt. It has been reported that pillared clay has a larger interlayer space, a higher surface area, better thermal stability, and higher surface acidity [19–21]. Al-pillared clays have been further confirmed to adsorb oxyanion pollutants, such as phosphate and arsenate [22,23], and organic anion dyes, such as acid orange II, and acid turquoise blue A [6]. Gil et al. [6] reported that the maximum adsorptions of montmorillonite towards acid orange II were 4.1 mg/g and 4.3 mg/g after Al-pillaring and Zr-pillaring, respectively. In addition, the maximum adsorption of bentonite toward acid turquoise blue A was 2.6 mg/g after Al-pillaring [24]. Furthermore, the reactive black adsorption capacity of Al-pillared montmorillonite increased from 12.0 to 40.8 mg/g [25]. Although recent studies have proven that inorganic pillared montmorillonite has the ability to remove organic acid dye, the adsorption mechanism related to the changes in the physical–chemical properties needs to be further studied in order to ascertain how the inorganic pillaring modification method improves the adsorption ability of montmorillonite towards organic acid dye.

In this study, we investigated how inorganic pillaring (Keggin  $Al_{13}$ ) modification leads to the improved adsorption ability of MMt towards MO. The physical–chemical properties of modified MMt were characterized and compared in order to ascertain the structural and surface changes after pillaring (intercalation and calcination), which may further affect the MO adsorption ability. The batch experiments were carried out to optimize the MO adsorption ability, and to understand the mechanisms of MO adsorption through kinetic and isotherm modeling studies. It is expected that natural MMt with a low cost can be used to fabricate high-quality adsorbents after modification using the methodologies developed in this study, and these technologies could be subsequently applied to modify multifunctional adsorbents.

## 2. Materials and Methods

### 2.1. Chemicals and Materials

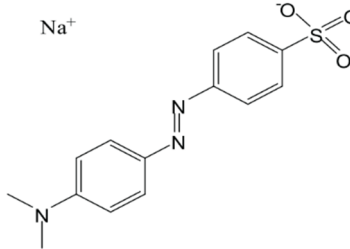
Calcium-rich montmorillonite was obtained from Inner Mongolia, China, and labeled as MMt. The purity of the MMt was >95%, which was certified by the Guangzhou Institute of Geochemistry, China. The chemical composition, structural formula, and particle size distribution of MMt are shown in Table 1. The MMt samples were used without further purification. The chemicals used in the synthesis and adsorption—including aluminum chloride, sodium hydroxide, and MO—were analytical grade. The aluminum chloride and MO were purchased from DAMAO Chemical Reagent Factory, and the sodium hydroxide was purchased from FUCHEN (Tianjin, China) Chemical Reagent Co., Ltd. The characterization of MO is listed in Table 2 [26–28].

**Table 1.** The chemical composition, structural formula, and particle size distribution of MMt.

Chemical composition	$SiO_2$ : 60.34%, $Al_2O_3$ : 16.83%, $MgO$ : 5.43%, $Fe_2O_3$ : 4.45%, $CaO$ : 2.83%, $TiO_2$ : 0.29%, $K_2O$ : 0.09%, $Na_2O$ : 0.06%. (LOI: 9.76%)
Structural formula *	$\left\{ \left( Al_{1.277} Mg_{0.488} Fe_{0.22}^{3+} Ti_{0.014}^{4+} \right) \left[ (Si_{3.971} Al_{0.029}) O_{10} \right] (OH)_2 \right\}$ $(Ca_{0.200} Mg_{0.044} K_{0.008} Na_{0.008}) \bullet n(H_2O)$
Particle size distribution	0.227–2.289 $\mu m$ , $D_x(50) = 1.221 \mu m$

\* calculated by chemical composition.

**Table 2.** Chemical structure and characteristics of MO.

Structure	
Molecular Weight (g/mol)	327.3
Molecular size (nm)	1.19 × 0.67 × 0.38 [26]

### 2.2. Synthesis of Al-Intercalated and Al-Pillared Montmorillonite

The synthesis method of the Keggin  $Al_{13}$  complex followed the procedure reported by Roca Jalil et al. [29]. The Keggin  $Al_{13}$  complex was prepared by adding 1 M sodium hydroxide drop-by-drop into 0.5 M aluminum chloride solution at a flow rate of around 3–4 mL/min under magnetic string at 60 °C, to obtain a final  $[OH^-]/[Al^{3+}]$  molar ratio of 2, followed by aging at 60 °C for 24 h. The Al-intercalated MMt and Al-pillared MMt were synthesized based on the method reported by Kumararaja et al. [30]. The Keggin  $Al_{13}$  complex was slowly added at a flow rate of around 3–4 mL/min into a 10% MMt dispersion (MMt/water = 1:10 in mass) under magnetic string at room temperature (~25 °C) to reach an end  $Al^{3+}$ /clay ratio of 10 mmol/g. The mixture was further aged under stirring for 24 h at room temperature (~25 °C), and then centrifuged at  $3790 \times g$ . The supernatant was decanted, and the obtained solid cake was washed with deionized water in order to remove electrolytes, such as chlorite ions. After that, the washed solid was dried at 80 °C for 15 h in an oven. The dried sample was Al-intercalated MMt, denoted as P-MMt. The newly formed P-MMt was subsequently calcined in a furnace under vacuum at various temperatures (200, 300, 400, 500, 600, 700, and 800 °C) for 2 h, at a 5 °C/min temperature ramping rate, based on the modified calcination method reported by Kumararaja et al. [30]. These Al-intercalated MMts, after calcination, were Al-pillared MMts named P-MMt- $C_x$  ( $C_x$  denotes the calcination temperature). The original MMt samples were also calcined at the same temperatures, which were labeled as MMt- $C_x$ .

### 2.3. Characterization

#### 2.3.1. X-ray Diffraction

The XRD patterns of the samples were obtained using the PANalytical X'Pert Pro MPD Power diffractometer with Cu  $K\alpha$  radiation at 40 kV and 40 mA. Around 20 mg of random powder sample was prepared and scanned from 3 to 70° (2 $\theta$ ) at a step size of 0.0167° and a scan rate of 1 s/step.

#### 2.3.2. Specific Surface Area (SSA)

The SSAs of the samples were calculated via the Brunauer, Emmett and Teller (BET) method, the Langmuir method, and the t-plot method, respectively, based on the  $N_2$  adsorption–desorption isotherms measured using a Beckman Colter SA 3100 at –196 °C. Prior to the measurement, a 200 mg sample was fully degassed under vacuum to remove the physically adsorbed moisture and other impurities.

#### 2.3.3. Thermogravimetric Analysis (TGA)

The mass change of the samples was determined using a Perkin Elmer Thermal Gravimetric Analyzer (TGA-6), operated at a heating rate of 10 °C/min from 100 to 950 °C under a high-purity flowing nitrogen atmosphere. The derivative thermogravimetric (DTG) curves were automatically derived from the TG curves.

### 2.3.4. Field Emission Scanning Electron Microscope (FE-SEM)

The FE-SEM photomicrographs and element composition of the samples were determined and recorded using a ZEISS EVO18 Scanning Electron Microscope (SEM) with an integrated Bruker flash 6130 energy dispersive X-ray analyser (EDX). The samples were spread and fixed onto carbon adhesive discs, and then plated with gold to enhance the conductivity.

### 2.4. Methyl Orange Adsorption

Batch experiments were carried out to determine the adsorption characteristics. In total, 20 mg adsorbents (the lowest adsorbent dose with the maximum amount of adsorption according to the pre-test) were prepared in order to optimize the kinetic test conditions. From the pre-test results, we found that 5 mg/L MO was appropriate to be used for adsorption when the equilibrium time was set at 640 min. In the batch experiment, 20 mg adsorbent was weighted into a centrifuge tube, and 50 mL MO with certain concentrations in the solution was added to the centrifuge tube. The centrifuge tube containing the mixture was agitated on a shaker at room temperature ( $\sim 25^\circ\text{C}$ ) at 300 rpm with different time intervals. After shaking, the solution and adsorbent were separated by a  $0.45\ \mu\text{m}$  membrane filter. The final pH of the sample was adjusted to the pH of the MO standard solution. The concentration of MO in the filtrate was analyzed using a UV-vis spectrometer at a wavelength of 464 nm. Each sample was examined triply. The MO adsorption capacity of the adsorbent can be calculated using the following equation:

$$q_t = V(C_i - C_t)/m \quad (1)$$

where  $q_t$  is the MO adsorption capacity of adsorbent at time  $t$ , mg/g;  $V$  is the volume of MO solution used in adsorption, L;  $C_i$  is the initial concentration of MO in solution, mg/L;  $C_t$  is the concentration of MO in solution at time  $t$ , mg/L; and  $m$  is the mass of the adsorbent used in the adsorption, g.

The adsorption kinetics experiment was carried out at room temperature. In total, 20 mg adsorbent was added to 50 mL 5 mg/L MO solution, and the MO concentration was measured at different time intervals (1–640 min) after agitating on a shaker at 300 rpm at room temperature ( $\sim 25^\circ\text{C}$ ). The adsorption isotherm studies were carried out at room temperature. In total, 20 mg adsorbents were added to 50 mL MO solutions with different concentrations (1–30 mg/L), and the mixtures were agitated on a shaker at 300 rpm for 640 min at room temperature ( $\sim 25^\circ\text{C}$ ). The determinations of the MO concentrations from the kinetic and isotherm experiments were the same as that described earlier for MO adsorption in this section.

### 2.5. Adsorption Kinetic and Isotherm Models

#### 2.5.1. Adsorption Kinetic Models

Adsorption kinetic models were studied in order to understand the rate of MO adsorption by the modified MMt with respect to the equilibration time. Pseudo-first-order (PFO) and pseudo-second-order (PSO) kinetic models were used to predict the adsorption rate of MO. If the adsorption process is fitted to the PFO kinetic model, it can be assumed to be physisorption [31]. The non-linearized form of the PFO model can be presented by the following equation [32]:

$$q_t = q_e(1 - e^{-k_1 t}) \quad (2)$$

where  $q_t$  is the adsorption capacity at time  $t$ , mg/g;  $q_e$  is the adsorption capacity at equilibrium, mg/g;  $t$  is the adsorption time, min; and  $k_1$  is the rate constant,  $\text{min}^{-1}$ .

If the adsorption process is fitted to the PSO kinetic model, it can be assumed to be chemisorption [33]. According to Ho and McKay [34], the non-linearized form of PSO model can be expressed as

$$q_t = k_2 q_e^2 t / (1 + k_2 q_e t) \quad (3)$$

where  $k_2$  is the PSO rate constant, (mg/g)/min.

### 2.5.2. Adsorption Isotherm

The basic assumption of the Langmuir isotherm model is that, when a monolayer of adsorbate is saturated on a homogenous surface of an adsorbent, the adsorbent can reach the maximum amount of adsorption [35]. The Langmuir model equation can be written as the following non-linearized form [36,37]:

$$q_e = q_m C_e K_L / (1 + C_e K_L) \quad (4)$$

where  $C_e$  is the equilibrium concentration of the adsorbate in the solution, mg/L;  $q_m$  is the monolayer adsorption of the adsorbate onto the adsorbent, mg/g; and  $K_L$  is the constant related to the free energy of adsorption, L/mg.

The Freundlich isotherm model is commonly used to express the adsorption which occurs on the heterogeneous surface of an adsorbent, with different affined adsorption sites towards the adsorbate [38]. This isotherm model can define the surface heterogeneity and the distribution of the adsorption sites and their energies [39]. This model can be expressed in the following equation:

$$q_e = k_F C_e^{1/n} \quad (5)$$

where  $k_F$  is the Freundlich constant related to the adsorption capacity of the adsorbent, (mg/g)/(mg/L)<sup>n</sup>, and  $1/n$  is the adsorption strength.

The Redlich–Peterson isotherm model, incorporating three parameters, combines both the Langmuir and Freundlich models, and explains the adsorption equilibrium results obtained from a wide range of adsorbate concentrations [40]. The Redlich–Peterson isotherm model is described in the following non-linearized equation [41]:

$$q_e = K_R C_e / (1 + \alpha_R C_e^\beta) \quad (6)$$

where  $K_R$  is the Redlich–Peterson isotherm constant; L/g;  $\alpha_R$  is also a constant, L/mg; and  $\beta$  is the exponent that lies between 0 and 1.

At relatively high concentrations of the adsorbate in an aqueous solution, the isotherm equation (Equation (6)) can be reduced to the Freundlich equation.

$$q_e = (K_R / \alpha_R) C_e^{1-\beta} \quad (7)$$

when  $\beta = 1$ , the Redlich–Peterson model can be reduced to the Langmuir equation. In contrast, when  $\beta = 0$ , the Redlich–Peterson model can be reduced to Henry's equation.

## 3. Results

### 3.1. X-ray Diffraction Analysis

The XRD pattern of MMt in Figure 1 shows that MMt is a highly pure calcium-montmorillonite with a very small amount of quartz, and that it exhibits a weak reflection at  $26.61^\circ$  (20). The reflection at  $5.73^\circ$  (20) is the 001 reflection with a 1.540 nm basal distance of MMt. After the Keggin  $Al_{13}$  complex was intercalated into the interlayer space, the basal distance ( $d_{001}$ ) of P-MMt increased from 1.540 to 1.847 nm. When P-MMt was calcined at  $400^\circ C$  (P-MMt-C400), the basal distance ( $d_{001}$ ) decreased slightly to 1.778 nm. The reflection at  $19.74^\circ$  (20) corresponds to the 020 reflection of MMt [42]. This is a two-dimensional non-basal reflection (hk) [43].

The XRD patterns of MMt and P-MMt calcined at different temperatures (200–800 °C) for 2 h are shown in Figure 2. It can be observed clearly that the basal distance of MMt decreases with increasing temperature. When the calcination temperature increased from 200 to 400 °C, the  $d_{001}$  value of MMt decreased from 1.540 to 1.518 nm, which was associated

with the reduction of the intensity. When the calcination temperature was 500 °C or over, the  $d_{001}$  value of MMt significantly decreased to 0.974 nm with a great shift in d-spacing (Figure 2B), which is the thickness of an individual MMt layer [44]. The XRD patterns of P-MMt calcined at different temperatures show that the intensity of the basal reflection was strongly diminished after calcination at 800 °C, but the basal distance decreased from 1.847 to 1.682 nm, with only a minor shift in d-spacing (Figure 2A).

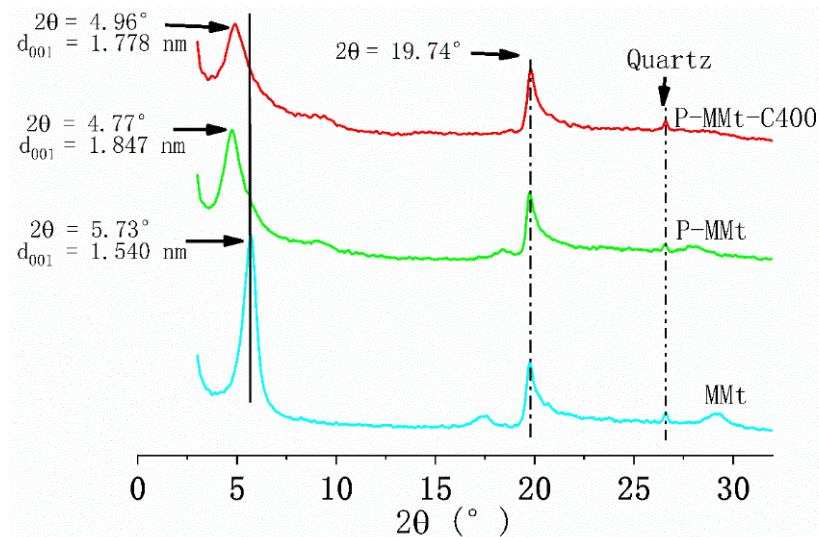


**Figure 1.** The XRD patterns of MMt, P-MMt, and P-MMt-C400.

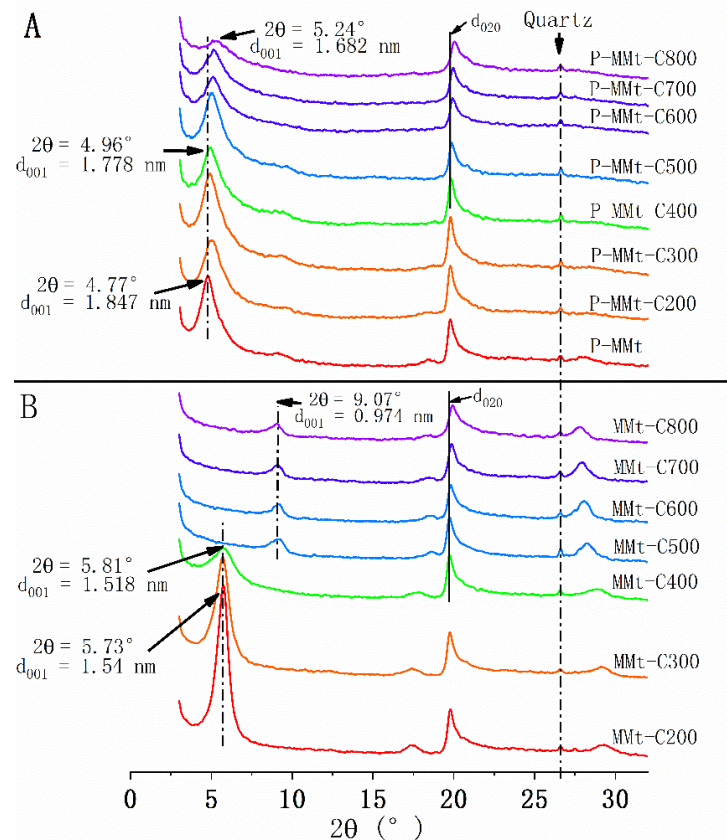


**Figure 2.** XRD patterns of P-MMt (A) and MMt (B) calcined at different temperatures.

### 3.2. Specific Surface Area and BET Adsorption–Desorption Isotherm

Figure 3 shows the effect of the calcination temperature on the BET SSA of P-MMt. The SSA of P-MMt slightly decreased after calcination at 200 °C, and then reached a maximum value of 293.7 m<sup>2</sup>/g after calcination at 400 °C. There was a significant increase of 231.0 m<sup>2</sup>/g in SSA of MMt compared with that of P-MMt (Table 3). When P-MMt was calcined at 600 °C and above, the SSA decreased significantly. Therefore, the N<sub>2</sub> adsorption–desorption isotherm and porosity of P-MMt-C400 were selected as the representative samples of P-MMt-C<sub>x</sub> for further study.

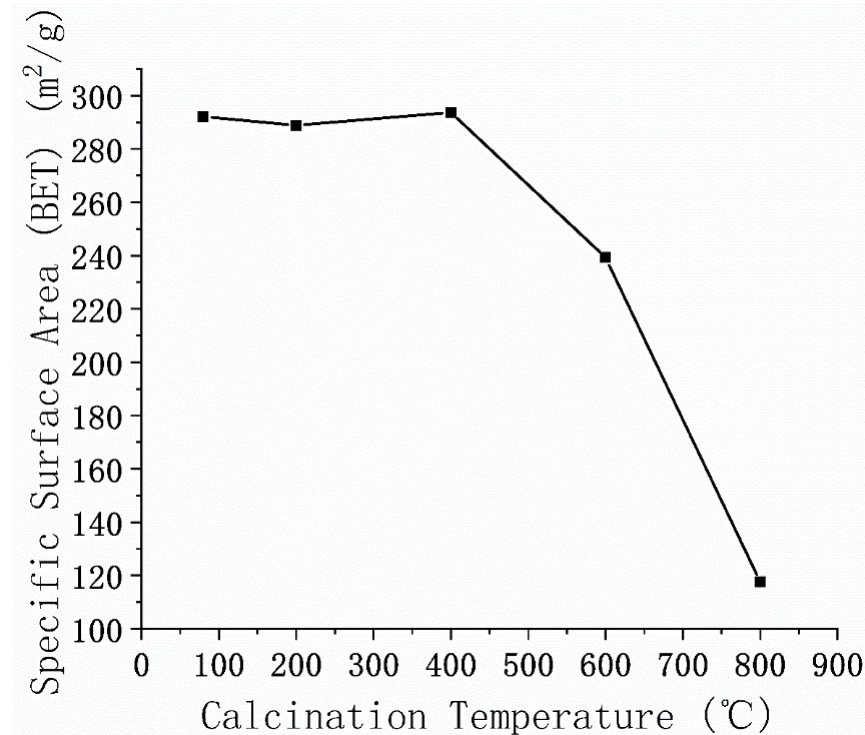


**Figure 3.** The effect of the calcination temperature on the SSA of P-MMt (no calcination at the first point).

**Table 3.** The textural properties of MMt, P-MMt and P-MMt-C400.

	S <sub>(BET)</sub> m <sup>2</sup> /g	S <sub>(Langmuir)</sub> m <sup>2</sup> /g	S <sub>(t-plot)</sub> m <sup>2</sup> /g	S <sub>(micro)</sub> * m <sup>2</sup> /g
MMt	61.1	66.1	42.7	18.6
P-MMt	292.1	358.3	59.5	238.1
P-MMt-C400	293.7	339.1	70.7	223.0

\* The S (micro) was calculated by the use of the t-plot theory.

Table 3 shows that the SSAs of P-MMt and P-MMt-C400 calculated by BET theory increased significantly, to 292.1 and 293.7 m<sup>2</sup>/g, compared to the 61.1 m<sup>2</sup>/g of MMt. In addition, P-MMt and P-MMt-C400 have a larger surface area of micropores (238.1 and 223.0 m<sup>2</sup>/g) than MMt (18.6 m<sup>2</sup>/g). Figure 4 shows that the volumes of micropores ranging from 0.40 to 1.20 nm in P-MMt and P-MMt-C400 are larger than that in MMt. The average micropore sizes of P-MMt (0.83 nm) and P-MMt-C400 (0.86 nm) become smaller than that of MMt (1.04 nm).

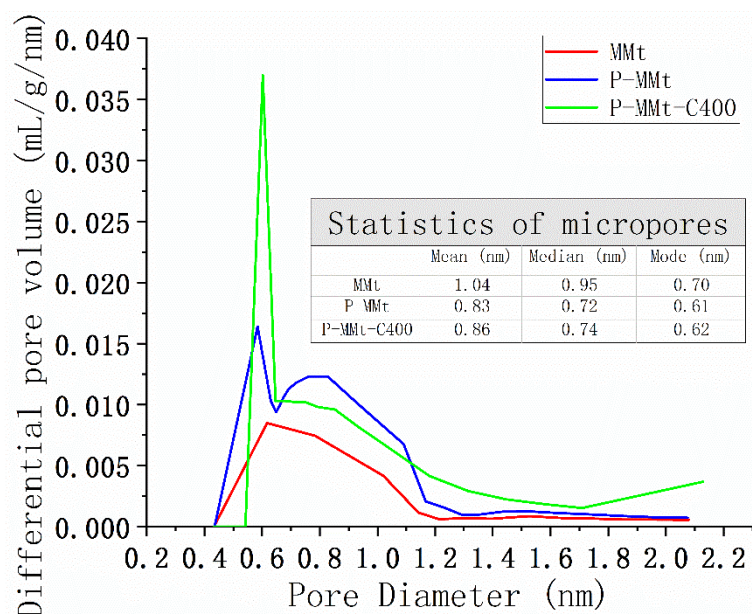


**Figure 4.** Micropore distribution of MMt, P-MMt, and P-MMt-C400 (calculated by the Horvath–Kawazoe model).

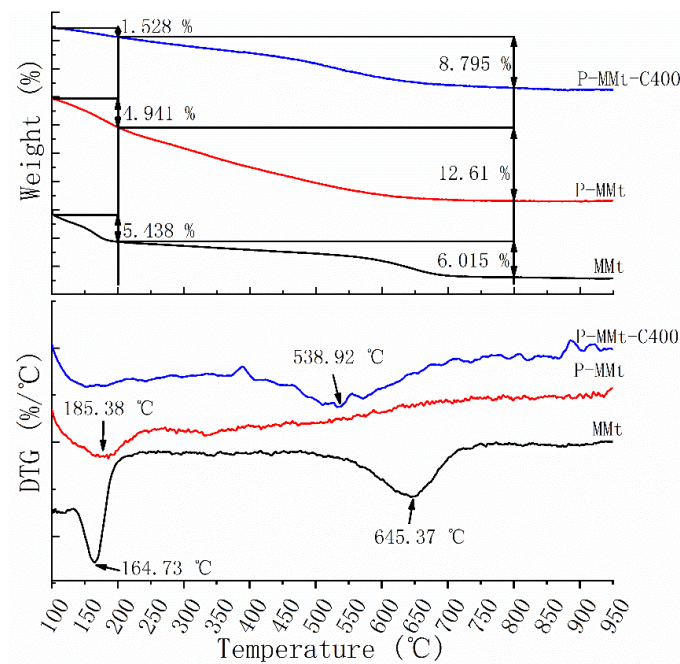
### 3.3. Thermogravimetric Analysis

Based on the results shown in the XRD and BET surface areas, P-MMt-C400 showed a perfect basal distance and the largest surface area. Therefore, in the thermogravimetric analysis, P-MMt-C400 was selected as a representative sample of P-MMt-C<sub>x</sub> to compare with MMt and P-MMt. Figure 5 shows the TG and DTG curves of MMt, P-MMt, and P-MMt-C400. There are two major mass losses, one below 200 °C and another between 200 and 800 °C. The first mass loss from 25 to 200 °C corresponds to the loss of free water adsorbed between the interlayers. This is called the dehydration process. The first major mass loss (5.4%) of MMt is shown below 200 °C, and is larger than those of P-MMt (4.9%) and P-MMt-C400 (1.5%). The second mass loss was the dehydroxylation of MMt (550–700 °C) and the dehydroxylation of the Keggin Al<sub>13</sub> complex in the interlayer of P-MMt (200–800 °C). Between 200 and 800 °C, the mass loss of MMt is 6.0%, which is less than those of P-MMt (12.6%) and P-MMt-C400 (8.7%). For P-MMt, the mass was continuously lost up to 17.5% when temperature was increased to 800 °C. On the other hand, the total mass loss of P-MMt-C400 was only 10.2%, which was less than those of MMt (11.4%) and P-MMt (17.5%) when heated up to 800 °C. According to the DTG curves shown in Figure 5, a peak is observed between 150 and 200 °C for MMt (center at 164 °C) and P-MMt (center at 185 °C), but no obvious peak is observed for P-MMt-C400 at the same temperature range. With the increasing temperature, a small broad band is shown between 400 and 700 °C, where the peak center at 538 °C and 645 °C is from P-MMt-C400 and MMt, respectively. However, no peak is recorded from P-MMt.

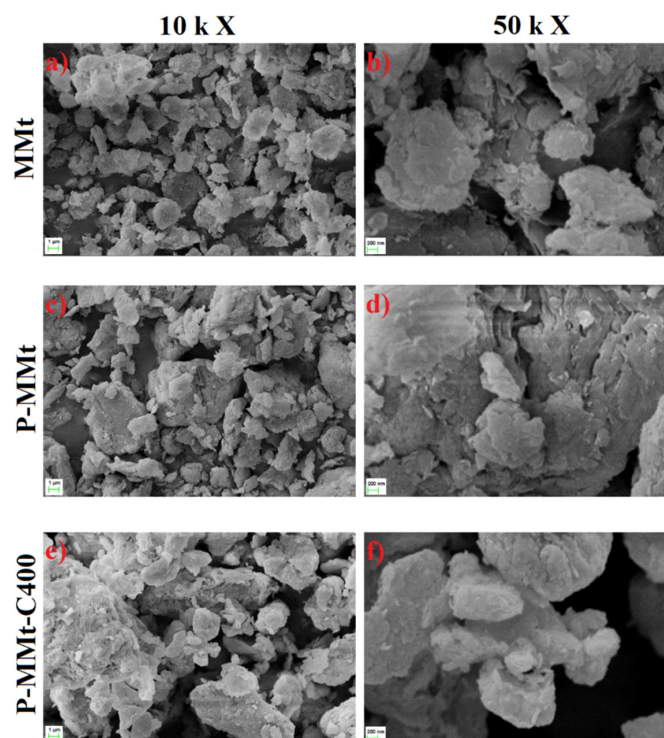
### 3.4. Micrographs of the Field Emission Scanning Electron Microscopy

Figure 6 shows the field emission scanning electron microscope (FE-SEM) images of MMt, P-MMt, and P-MMt-C400. The MMt has larger aggregates of plates with a platy structure (Figure 6a,b). The surfaces of the particles are smooth, with clear and rough edges. After the intercalation of Keggin Al<sub>13</sub>, the morphology (Figure 6c,d) was still a platy structure, but the surfaces became coarser, with more folds. The FE-SEM images (Figure 6e,f) show that P-MMt-C400, which is calcined, has more irregular shapes of aggregates, and its edges become smooth together with the formation of the amorphous phase on the particle surfaces. In addition, the Al/Si ratio is calculated from the chemical composition, which is determined by the coupling Energy Dispersive X-ray Detector (EDX) (Table A1). The

Al/Si ratio of P-MMt was increased from 0.29 to 0.53 after modification, and the Al/Si ratio remained at 0.53 after calcination (P-MMt-C400).



**Figure 5.** The TG and DTG curves of MMt, P-MMt, and P-MMt-C400.

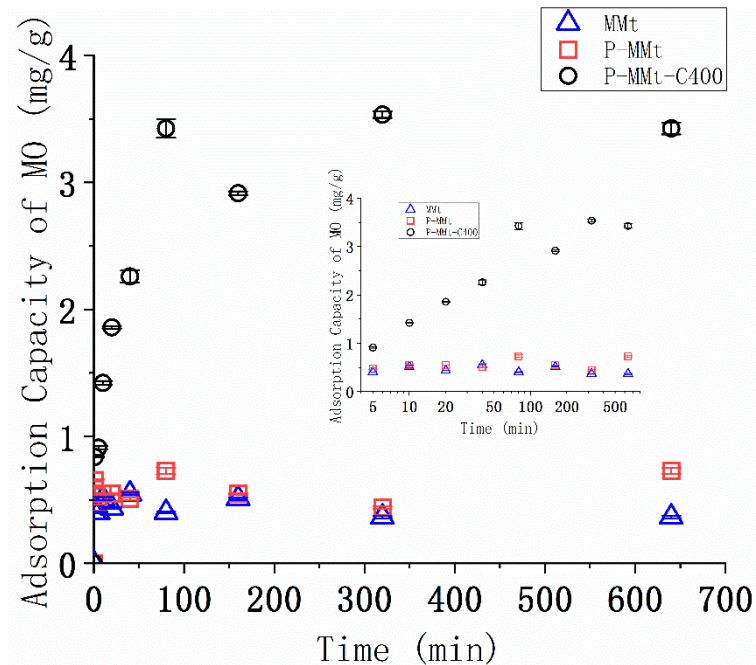


**Figure 6.** Surface structure and particle size of (a,b) MMt, (c,d) P-MMt, and (e,f) P-MMt-C400 in the field emission scanning electron microscope (FE-SEM) images.

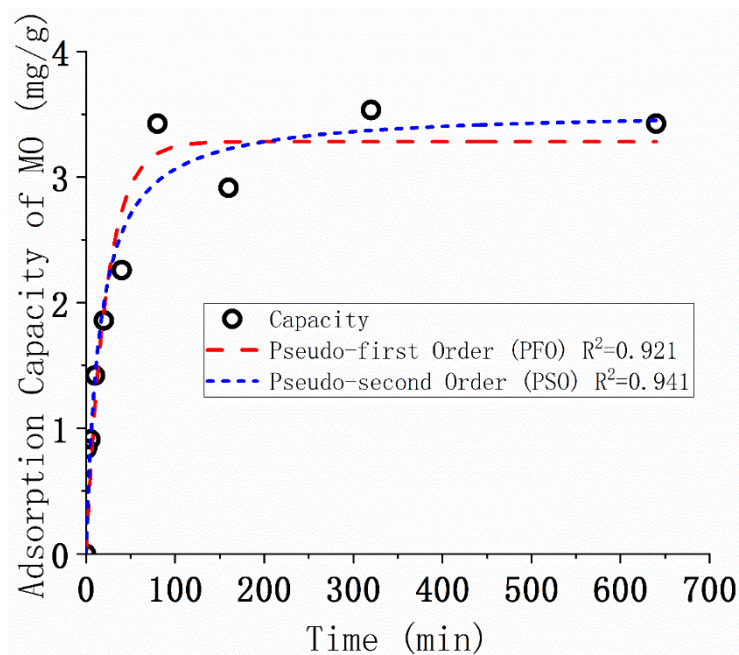
### 3.5. Kinetics of the MO Adsorption

Table A2 and Figure 7 show that MMt and P-MMt adsorbed less MO compared to P-MMt-C400. The amount of MO adsorbed onto P-MMt-C400 increased with time, reaching a maximum value at about 100–200 min, and thereafter it remained in a state of dynamic

equilibrium. The MO adsorption of P-MMt-C400 was rapid in the first 50 min, reaching the largest amount, and then fluctuated or decreased gradually with the increasing contact time. Thus, P-MMt-C400 was used in the study of adsorption for model fitting because it had the best adsorption behavior.



**Figure 7.** The MO adsorption (50 mL of 5 mg/L solution) of MMt, P-MMt, and P-MMt-C400 at different contact time intervals; SD is added as an error bar to each point, n = 3. The x-axis of the inserted figure is in log scale.



**Figure 8.** MO adsorption of P-MMt-C400 in different contact time intervals, fitted by pseudo-first-order and pseudo-second-order models.

The PFO and PSO models in non-linear form were applied for fittings with the data from the adsorption kinetic of P-MMt-C400 (Figure 8), and the related parameters of fitted PFO and PSO are shown in Table 4. The PSO shows better fitting with  $R^2 = 0.941$ , which

is a higher than the value ( $R^2 = 0.921$ ) obtained from the fitting of PFO. According to the parameters of PSO, the MO adsorption capacity of P-MMt-C400 is 3.42 mg/g from the experiment, which approaches the equilibrium adsorption capacity (3.53 mg/g) calculated by PSO. The adsorption rate of MO onto P-MMt-C400 is 0.0184 (mg/g)/min, obtained from the PSO rate constant.

**Table 4.** Parameters of the pseudo-first-order and pseudo-second-order kinetic models fitted by the MO adsorption data of P-MMt-C400.

Kinetic Model	Parameter	
	$q_{\text{exp}}$ (mg/g) at 640 min	$3.42 \pm 0.04$
Pseudo-first-order (PFO)	$q_e$ (mg/g)	$3.28 \pm 0.19$
	$k_1$ ( $\text{min}^{-1}$ )	$0.0443 \pm 0.0100$
	$R^2$	0.921
	$q_e$ (mg/g)	$3.53 \pm 0.20$
Pseudo-second-order (PSO)	$k_2$ (mg/g)/min	$0.0184 \pm 0.0056$
	$R^2$	0.941

### 3.6. Isotherms of MO Adsorption

The relationships between the equilibrium concentrations of MO and the adsorption capacities of Mt, P-MMt, and P-MMt-C400 are shown in Table A3 and Figure 9. They show that the adsorption capacity of P-MMt-C400 is significantly different from those of MMt and P-MMt, which correspond identically to the results of adsorption kinetics. Therefore, three isotherm models (the Langmuir model, the Freundlich model, and the Redlich–Peterson model) were used to study the MO adsorption of P-MMt-C400.

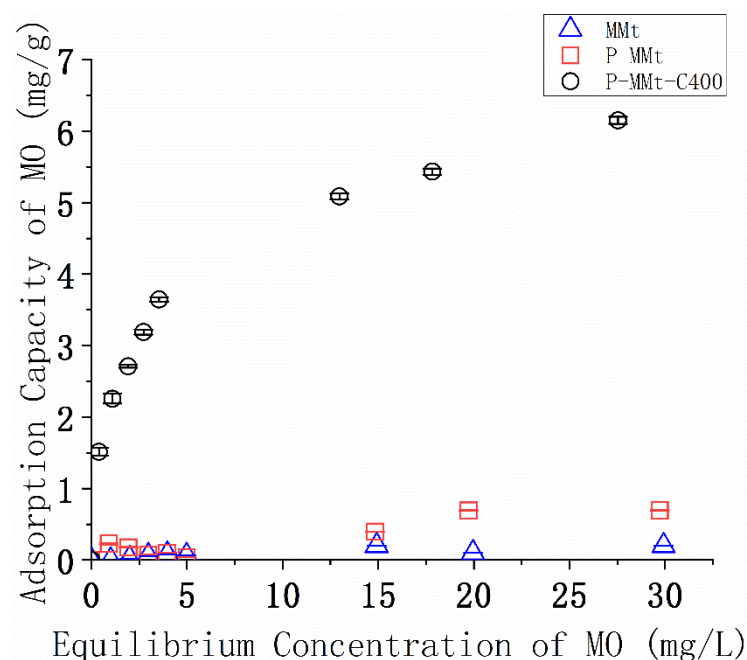


**Figure 9.** MO adsorption by MMt, P-MMt, and P-MMt-C400 in different equilibrium concentrations of MO; SD is added to each point as an error bar,  $n = 3$ .

Three adsorption isotherm models (Langmuir, Freundlich, and Redlich–Peterson) were perfectly fitted by the MO adsorption data of P-MMt-C400, with high correlation coefficients ( $R^2 = 0.977$ , 0.994, and 0.998, respectively) (Figure 10).

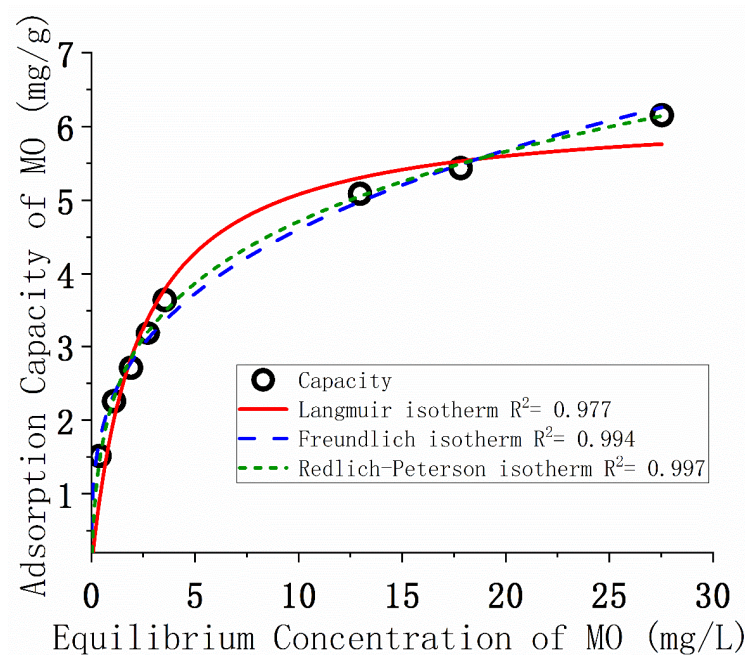


**Figure 10.** MO adsorption by P-MMt-C400 in different equilibrium concentrations, fitted by the Langmuir, Freundlich, and Redlich–Peterson isotherm models.

According to Table 5, the adsorption of MO by P-MMt-C400 was a better fitting for the Freundlich isotherm model ( $R^2 = 0.994$ ) than for the Langmuir model ( $R^2 = 0.977$ ). In the Freundlich isotherm, the value of  $1/n$  is 0.30, approaching zero. Although the Langmuir model is inferior to the Freundlich model in the fitting of the MO adsorption isotherms, it still has a high correlation coefficient (0.977). Thus, the value of  $q_m$  obtained from the Langmuir model can be used to predict or represent the maximum adsorption capacity of P-MMt-C400, which is 6.23 mg/g. Compared to the maximum adsorption capacity (0.25 mg/g) of MMt calculated by Langmuir fitting in MO adsorption by MMt, the MO adsorption capacity of P-MMt-C400 was around 25 times larger than that of MMt. In this study, the Redlich–Peterson model was the best fit for MO adsorption by P-MMt-C400 with  $R^2 = 0.998$ , compared to the Langmuir and Freundlich models.

**Table 5.** Parameters of the Langmuir, Freundlich, and Redlich–Peterson models fitted to the adsorption of MO onto P-MMt-C400.

Isotherm Model	Parameter	P-MMt-C400
Langmuir	$q_m$ (mg/g)	$6.23 \pm 0.27$
	$K_L$ (L/mg)	$0.436 \pm 0.066$
	$R^2$	0.977
Freundlich	$K_F$ ((mg/g)/(mg/L) <sup>n</sup> )	$2.29 \pm 0.07$
	$1/n$	$0.30 \pm 0.01$
	$R^2$	0.994
Redlich-Peterson	$K_R$ (L/g)	$9.87 \pm 2.81$
	$\alpha_R$ (L/mg)	$3.43 \pm 1.21$
	$\beta$	$0.76 \pm 0.02$
	$R^2$	0.998

## 4. Discussion

### 4.1. Intercalation of the Modifier into MMt

The shifts of the basal distance in the XRD results (Figure 1) indicate that the Keggin  $Al_{13}$  complex was successfully intercalated into the interlayer of MMt by increasing the interlayer space of MMt after intercalation. In addition, the FE-SEM images (Figure 6c,d) show that the shape is still a platy structure after the Keggin  $Al_{13}$  complex modification, indicating that the modification did not affect the structure layer. The coarser surfaces and clear folds shown in P-MMt (Figure 6c,d) are due to the adhesion of the Keggin  $Al_{13}$  complex on the surface and the increase of the interlayer space after modification. The amorphous surface of P-MMt-C400 (Figure 6e,f) is resulted from the formation of amorphous phases, which are the poor crystalline phases, due to calcination. The interlayer space of P-MMt is about the size of the Keggin  $Al_{13}$  complex, which is 0.873 nm, calculated by subtracting the thickness (0.974 nm) of an individual MMt layer from the basal distance (1.847 nm) of P-MMt. The size of the Keggin  $Al_{13}$  complex intercalated into MMt is in agreement with the average diameter of Keggin  $Al_{13}$  cations (~0.9 nm) [45]. Figure 1 shows that the 020 reflection is not affected after pillaring modification, indicating that the pillaring modification process does not affect the layer structure of MMt, but does affect the interlayer of MMt. In addition, the increased Al/Si ratio from MMt to P-MMt and the unchanged Al/Si ratio between P-MMt and P-MMt-C400 indicated that the Keggin  $Al_{13}$  complex was successfully added into MMt, and that the calcination has no negative effect on the loaded amount of the Keggin  $Al_{13}$  complex in P-MMt-C400.

### 4.2. Thermal Stability of Modified MMt

According to the XRD results (Figure 2), when the calcination temperature is over 400 °C (500–800 °C), the  $d_{001}$  value of MMt significantly decreases to 0.974 nm, indicating that the interlayer space of MMt starts to collapse over 400 °C. With an increasing calcination temperature (up to 800 °C), in contrast, the basal distance of P-MMt changes from 1.847 to 1.682 nm, with a decrease of 0.165 nm only, compared to the 0.566 nm of MMt, indicating that the interlayer distance of Al-pillared MMt is more stable than the precursor MMt against the increasing calcination temperature. This suggests that the aluminum oxide pillar formed from the Keggin  $Al_{13}$  complex in the interlayer of P-MMt supports the interlayer structure and prevents it from decomposition, thus providing better thermal stability [19,29]. However, the 020 reflection peak in both MMt and P-MMt started to shift to higher  $2\theta$  degree when the calcination temperature at 600 °C (Figure 2). It might be due to the dehydroxylation of the MMt layer during calcination.

The total mass loss of P-MMt is larger than that of MMt, but no peak of mass loss was shown between 200 and 800 °C, suggesting that there are no obvious structural decomposition stages shown for P-MMt. This indicates that P-MMt shows better thermal stability than its precursor, MMt. In TGA, when the temperature reaches 400 °C and over, which is the same temperature as the calcination temperature of P-MMt-C400, it shows the beginning of a peak of mass loss from 400 to 680 °C with a center of 538 °C, possibly due to the incomplete transformation of the Keggin  $Al_{13}$  complex to aluminum oxides. The higher total amounts of mass loss recorded from P-MMt (12.61%) and P-MMt-C400 (8.795%) than from MMt (6.015%), particularly the mass losses in higher calcination temperatures for P-MMt and P-MMt-C400, are believed to be mainly due to the Keggin  $Al_{13}$  incorporated into the mineral structure associated with the increase in its dehydroxylation temperature towards thermal stability. The peak at 500–725 °C, with a center of 645 °C, is attributed to the structural transformation of MMt [43], where the temperature at the beginning of this peak (i.e., 500 °C) corresponds to the great shift in the d-spacing of the XRD pattern, as shown by MMt-C500 in Figure 2B.

### 4.3. Surface Area of Modified MMt

The increase in the BET surface area (Table 3) of Al-intercalated MMt (P-MMt) and Al-pillared MMt (P-MMt-C400) is mainly due to the micropores (0.6–2.0 nm), with three

possible reasons: (a) the micropores are formed from the voids in the Keggin  $Al_{13}$  complex that is intercalated into MMt, and from the voids between two Keggin  $Al_{13}$  complexes; (b) the micropores in the interlayer of MMt could be detected after the Keggin  $Al_{13}$  complex expanded the interlayer of MMt; and (c) the particles of P-MMt are more dispersed and the surfaces are coarser than those of MMt, which can be observed in SEM images (Figure 6c–f). According to Figure 3, when P-MMt was calcined at 600 °C and above, the SSA of P-MMt significantly decreased. In addition, Figure 2A shows that when the calcination increased to 600 °C, the  $d_{001}$  peak shifted to higher  $2\theta$  degree and the intensity of the  $d_{001}$  peak decreased. Therefore, the decreasing SSA is related to the changes of the Keggin  $Al_{13}$  complex in the interlayer with the increasing temperature. This might be due to the continuous loss of hydroxyl groups of the Keggin  $Al_{13}$  complex, which provides voids, resulting in the decrease in micropores of P-MMt- $C_x$ , and consequently the decrease in the surface area.

Compared to the surface area calculated by BET, the surface areas calculated by the Langmuir theory of P-MMt and P-MMt-C400 are 20% larger. This is because the micropores, even though they contributed to the increase in surface area, may restrict multiple-layer adsorption, influencing the BET calculation. Although BET calculation is good for the computation of finely divided porous materials, in the case of the samples used in this work, it is better to use the Langmuir theory to determine the SSA for the P-MMt series (Table 3) [46,47].

#### 4.4. MO Adsorption of Modified MMt

After modification, the maximum adsorption ability of P-MMt towards MO is improved significantly, compared to that of the precursor MMt. The hydrophilic property of MMt results in it being less attracted to non-polar organic compounds, performing poorly in MO adsorption [10,48,49]. In addition, the highly negatively charged surface of MMt may hinder the MO (anionic dye) moving to MMt by repulsion. After Al-pillaring, the maximum MO adsorption ability increased from 0.25 mg/g (MMt) to 6.23 mg/g (P-MMt-C400). It has been reported that strong Lewis acidity may arise from the coordinately unsaturated aluminum centers on the aluminum pillars [48,49]; thus, the Lewis acidity sites from the aluminum coordination in Al-pillared MMt (e.g., P-MMt-C400) can provide adsorption sites to attract MO onto their surface.

If we consider that the MO molecules were horizontally adsorbed into the porous structure of the adsorbent, the cross-section of the MO molecule is  $0.67 \times 0.38$  nm (Table 2). In order to adsorb the MO in the horizontal orientation, the size of the pore should be at least 0.67 nm. In addition, it has been reported that pollutant molecules can be adsorbed into pores with a diameter 1.3–1.8 times that of the pollutant [50]. If the maximum value (1.8 times) is taken, the minimum pore size adsorbing the MO in the horizontal orientation is ~1.2 nm [6]. However, according to Figure 4, the increase in the surface area of Al-pillared MMt is mainly attributed to micropores ranging from 0.4 to 1.2 nm. Therefore, even under these conditions, the higher surface area of Al-pillared MMt (P-MMt and P-MMt-C400) could not provide more available adsorption sites to adsorb more MO even though it has a larger surface area due to the smaller size of its micropores. In contrast, our results indicate that the improvement of the MO adsorption ability of Al-pillared MMt is due to the property of the Keggin  $Al_{13}$  complex and the increase in the surface area contributed by micropores larger than 1.2 nm. It is therefore safe to conclude that the MO is adsorbed onto the surface of the Keggin  $Al_{13}$  complex which is in the interlayer, edge, and bared surface of MMt and its modified products, and this absorption can be associated with the contribution from the increase in meso- and macro-pores, and even micropores larger than 1.2 nm after modification.

The kinetics fitting results (Table 4) show that the adsorption kinetic of P-MMt-C400 is better fitted to the PSO, indicating that the MO adsorption processes of these modified MMts are supposed to be dominated by chemisorption. Further interpretation of the kinetic data shows that the interaction between P-MMt-C400 and MO is electrostatic. According to

the isotherm fittings (Table 5), three adsorption isotherm models (Langmuir, Freundlich, and Redlich–Peterson) are perfect fits for the data of MO adsorption by P-MMt-C400. Recent studies have reported that either the Langmuir model or the Freundlich model fits the organic dye contaminant adsorption on modified clay [6,8,51]. The difference of  $R^2$  between the PSO and PFO model fittings is not significant in this study. MO probably interacts with the modified MMt by mixed interaction modes, as reflected by the low value of the Freundlich  $1/n$  parameter, which is strongly related to the energetic heterogeneity of the adsorption processes. Future study is therefore desired in order to fully understand the reaction mechanism.

In this study, the Redlich–Peterson model was better fitted to the MO adsorption isotherm of P-MMt-C40 than the Langmuir and Freundlich models. The  $\beta$  value of the Redlich–Peterson model for MO adsorption by P-MMt-C400 is 0.76, which is not close to 1, indicating that the isotherms are close to the Freundlich model, and suggesting that the adsorption process of P-MMt-C400 is heterogeneous multilayer adsorption.

#### 4.5. Comparison of the Anionic Dye Removal with Other Adsorbents

Table 6 shows the maximum adsorption abilities of inorganic-pillared montmorillonites towards anionic dye removal. It shows that the anionic dye adsorption ability of Al-pillared montmorillonite in this study is better than those in most of previous studies. However, Al-pillared montmorillonite still has a relatively weaker adsorption ability than montmorillonite pillared with other type of metals. This will be the target of improvement in future study.

**Table 6.** The maximum adsorption ability of inorganic-pillared montmorillonite towards anionic dye.

Absorbent	Anionic Dye	$q_{\max}$ (mg/g)	$q_{\max}$ (mmol/g)	Reference
Al-pillared montmorillonite	Methyl Orange	6.23	0.0190	this study
Zr-pillared bentonite (without calcination)	Methyl Orange	44.13	0.1348	[51]
Al-pillared montmorillonite	Reactive Black 5	40.8	0.0411	[25]
Al-pillared bentonite (without calcination)	Acid Turquoise Blue A	2.639	0.0038	[24]
Al-pillared montmorillonite	Orange II	4.1	0.0117	[6]
Zr-pillared montmorillonite	Orange II	4.3	0.0123	[6]
Cr-pillared montmorillonite	Supranol Yellow 4GL	58.47	0.0526	[52]

## 5. Conclusions

The pillaring modification of MMt through Al intercalation and calcination at various temperatures was successfully achieved in this study. The modified MMt reveals a higher SSA and more thermal stability than the precursor MMt, and the MO adsorption ability is consequently optimized. The increase in SSA is due to the increase in porosity, and the enlargement of interlayer space resulted from the Keggin  $Al_{13}$  complex, together with the variation of surface properties such as structural defects generated during thermal processes. The intercalation of Keggin  $Al_{13}$  into the interlayer of MMt not only plays an important role in supporting the structure of modified MMt against thermal decomposition but also provides more affinitive sites for MO adsorption, which are believed to be the stronger Lewis acidic surfaces to attract MO anionic dye. One of the most important findings in this study, in addition to those stated above, is that not all of the the pores developed during modification contribute to adsorb MO; only those larger than  $\sim 1.2$  nm perform this function.

The Al-pillared MMt in this study could be applied as an adsorbent in a water purification system to remove MO or other dye elements. In order to examine the practical

use in water purification, the adsorption abilities of Al-pillared MMt towards different pollutants, the regeneration of Al-pillared MMt, and the adsorption abilities of Al-pillared MMt applied in the water purification will be studied in future studies.

**Author Contributions:** Experimental design, J.C., L.S. and H.R.; methodology setup, J.C.; process of the experiment, J.C.; data acquisition, analysis, and interpretation, J.C.; technical support, J.L., Y.Z. and Z.W.; data validation, L.S. and H.R.; writing—original draft preparation, J.C.; writing—review and editing, Y.J., L.S., Z.C., J.L., Y.Z., Z.W., C.L. and H.R.; supervision, H.R.; project administration, H.R.; funding acquisition, H.R. and Y.J. All authors have read and agreed to the published version of the manuscript.

**Funding:** This research was financially supported by Guangdong Province High Education Key Platform and Research Project 2020, Project No. 2020ZDZX1022; Guangdong High Education Youth Creation Grant, Project No. 2020KQNCX099; and the Beijing Normal University–Hong Kong University United International College (UIC), under the Re-search Projects R5202018, R201805 and R6014.

**Institutional Review Board Statement:** Not applicable.

**Informed Consent Statement:** Not applicable.

**Data Availability Statement:** Not applicable.

**Conflicts of Interest:** The funders had no role in the design of the study; in the collection, analyses, or interpretation of data; in the writing of the manuscript, or in the decision to publish the results.

## Appendix A

**Table A1.** Chemical compositions of MMt, P-MMt, and P-MMt-C400 (determined by EDX).

Sample	Element Weight %									Al/Si
	C	O	Mg	Al	Si	Ca	Ti	Fe	Other	
MMt	3.7	47.44	2.48	6.31	21.28	1.88	0.30	3.57	13.05	0.29
P-MMt	20.31	41.42	1.35	6.67	12.45			1.56	16.24	0.53
P-MMt-C400	10.55	41.03	1.68	7.95	14.8			2.1	21.90	0.53

**Table A2.** The MO adsorption capacities of MMt, P-MMt, and P-MMt-C400 in various times.

Time (min)	MO Adsorption Capacity					
	MMt		P-MMt		P-MMt-C400	
		SD		SD		SD
1	0.40087	0.00549	0.65598	0.00969	0.83819	0.00289
5	0.40087	0.00615	0.47376	0.01141	0.91108	0.01427
10	0.51020	0.01151	0.54665	0.00906	1.42128	0.01547
20	0.43732	0.00677	0.54665	0.00664	1.85860	0.01003
40	0.54665	0.01006	0.51020	0.01104	2.25948	0.04722
80	0.40087	0.00835	0.72886	0.02620	3.42566	0.07279
160	0.51020	0.00886	0.54665	0.00747	2.91545	0.01501
320	0.36443	0.00848	0.43732	0.01080	3.53499	0.02636
640	0.36443	0.00997	0.72886	0.02367	3.42566	0.04676

**Table A3.** The MO equilibrium adsorption capacities of MMT, P-MMt, and P-MMt-C400.

MMt			P-MMt			P-MMt-C400		
$C_e$	$q_e$	SD	$C_e$	$q_e$	SD	$C_e$	$q_e$	SD
1.0076	-	-	0.90845	0.22887	0.01042	0.39437	1.5140	0.05608
1.9920	0.02000	$3.4077 \times 10^{-4}$	1.92913	0.17717	0.00419	1.09693	2.2576	0.06830
2.9758	0.06048	$2.3179 \times 10^{-4}$	2.96875	0.07813	$4.3908 \times 10^{-4}$	1.91549	2.7112	0.02008
3.9673	0.08163	$2.4489 \times 10^{-4}$	3.96000	0.10000	$7.0265 \times 10^{-4}$	2.72422	3.1894	0.03525
4.9754	0.06127	$1.4228 \times 10^{-4}$	4.98408	0.03981	$2.3133 \times 10^{-4}$	3.54167	3.6458	0.03390
14.920	0.19947	$5.9841 \times 10^{-4}$	14.8412	0.39683	0.00218	12.965	5.0872	0.04070
19.959	0.10040	$8.5706 \times 10^{-4}$	19.7233	0.69170	0.00572	17.826	5.4347	0.04348
29.920	0.19947	0.00160	29.7214	0.69629	0.00557	27.539	6.1523	0.04922

## References

- Zhou, Y.; Lu, J.; Zhou, Y.; Liu, Y. Recent advances for dyes removal using novel adsorbents: A review. *Environ. Pollut.* **2019**, *252*, 352–365. [\[CrossRef\]](#) [\[PubMed\]](#)
- Darwish, A.A.A.; Rashad, M.; AL-Aoh, H.A. Methyl orange adsorption comparison on nanoparticles: Isotherm, kinetics, and thermodynamic studies. *Dye. Pigment.* **2019**, *160*, 563–571. [\[CrossRef\]](#)
- Gong, R.; Ye, J.; Dai, W.; Yan, X.; Hu, J.; Hu, X.; Li, S.; Huang, H. Adsorptive removal of methyl orange and methylene blue from aqueous solution with finger-citron-residue-based activated carbon. *Ind. Eng. Chem. Res.* **2013**, *52*, 14297–14303. [\[CrossRef\]](#)
- Nasar, A.; Mashkoo, F. Application of polyaniline-based adsorbents for dye removal from water and wastewater—A review. *Environ. Sci. Pollut. Res.* **2019**, *26*, 5333–5356. [\[CrossRef\]](#)
- Bhatia, D.; Sharma, N.R.; Singh, J.; Kanwar, R.S. Biological methods for textile dye removal from wastewater: A review. *Crit. Rev. Environ. Sci. Technol.* **2017**, *47*, 1836–1876. [\[CrossRef\]](#)
- Gil, A.; Assis, F.C.C.; Albeniz, S.; Korili, S.A. Removal of dyes from wastewaters by adsorption on pillared clays. *Chem. Eng. J.* **2011**, *168*, 1032–1040. [\[CrossRef\]](#)
- Katheresan, V.; Kannedo, J.; Lau, S.Y. Efficiency of various recent wastewater dye removal methods: A review. *J. Environ. Chem. Eng.* **2018**, *6*, 4676–4697. [\[CrossRef\]](#)
- Kausar, A.; Iqbal, M.; Javed, A.; Aftab, K.; Nazli, Z.I.H.; Bhatti, H.N.; Nouren, S. Dyes adsorption using clay and modified clay: A review. *J. Mol. Liq.* **2018**, *256*, 395–407. [\[CrossRef\]](#)
- Adebajo, M.O.; Frost, R.L.; Klopogge, J.T.; Carmody, O.; Kokot, S. Porous Materials for Oil Spill Cleanup: A Review of Synthesis. *J. Porous Mater.* **2003**, *10*, 159–170. [\[CrossRef\]](#)
- Liu, C.; Wu, P.; Zhu, Y.; Tran, L. Simultaneous adsorption of Cd<sup>2+</sup> and BPA on amphoteric surfactant activated montmorillonite. *Chemosphere* **2016**, *144*, 1026–1032. [\[CrossRef\]](#)
- Rathnayake, S.I.; Xi, Y.; Frost, R.L.; Ayoko, G.A. Structural and thermal properties of inorganic-organic montmorillonite: Implications for their potential environmental applications. *J. Colloid Interface Sci.* **2015**, *459*, 17–28. [\[CrossRef\]](#)
- De Pablo, L.; Chávez, M.L.; Abatal, M. Adsorption of heavy metals in acid to alkaline environments by montmorillonite and Ca-montmorillonite. *Chem. Eng. J.* **2011**, *171*, 1276–1286. [\[CrossRef\]](#)
- Chen, C.; Liu, H.; Chen, T.; Chen, D.; Frost, R.L. Applied Clay Science An insight into the removal of Pb (II), Cu (II), Co (II), Cd (II), Zn (II), Ag (I), Hg (I), Cr (VI) by Na (I) -montmorillonite and Ca (II) -montmorillonite. *Appl. Clay Sci.* **2015**, *118*, 239–247. [\[CrossRef\]](#)
- Uddin, M.K. A review on the adsorption of heavy metals by clay minerals, with special focus on the past decade. *Chem. Eng. J.* **2017**, *308*, 438–462. [\[CrossRef\]](#)
- Almeida, C.A.P.; Debacher, N.A.; Downs, A.J.; Cottet, L.; Mello, C.A.D. Removal of methylene blue from colored effluents by adsorption on montmorillonite clay. *J. Colloid Interface Sci.* **2009**, *332*, 46–53. [\[CrossRef\]](#)
- Roca Jalil, M.E.; Baschini, M.; Sapag, K. Influence of pH and antibiotic solubility on the removal of ciprofloxacin from aqueous media using montmorillonite. *Appl. Clay Sci.* **2015**, *114*, 69–76. [\[CrossRef\]](#)
- Wu, Q.; Li, Z.; Hong, H.; Yin, K.; Tie, L. Adsorption and intercalation of ciprofloxacin on montmorillonite. *Appl. Clay Sci.* **2010**, *50*, 204–211. [\[CrossRef\]](#)
- Hui, C.; Keeling, J. Applied Clay Science Fundamental and applied research on clay minerals: From climate and environment to nanotechnology. *Appl. Clay Sci.* **2013**, *74*, 3–9. [\[CrossRef\]](#)
- Liu, Y.; Dong, C.; Wei, H.; Yuan, W.; Li, K. Adsorption of levofloxacin onto an iron-pillared montmorillonite (clay mineral): Kinetics, equilibrium and mechanism. *Appl. Clay Sci.* **2015**, *118*, 301–307. [\[CrossRef\]](#)
- Okoye, I.P.; Obi, C. Synthesis and Characterization of Al-Pillared Bentonite Clay Minerals. *Res. J. Appl. Sci.* **2011**, *6*, 447–450. [\[CrossRef\]](#)
- Qin, Z.; Yuan, P.; Yang, S.; Liu, D.; He, H.; Zhu, J. Silylation of Al<sup>3+</sup>-intercalated montmorillonite with trimethylchlorosilane and their adsorption for Orange II. *Appl. Clay Sci.* **2014**, *99*, 229–236. [\[CrossRef\]](#)

22. Kasama, T.; Watanabe, Y.; Yamada, H.; Murakami, T. Sorption of phosphates on Al-pillared smectites and mica at acidic to neutral pH. *Appl. Clay Sci.* **2004**, *25*, 167–177. [[CrossRef](#)]
23. Lenoble, V.; Bouras, O.; Deluchat, V.; Serpaud, B.; Bollinger, J.C. Arsenic adsorption onto pillared clays and iron oxides. *J. Colloid Interface Sci.* **2002**, *255*, 52–58. [[CrossRef](#)] [[PubMed](#)]
24. Hao, Y.F.; Yan, L.G.; Yu, H.Q.; Yang, K.; Yu, S.J.; Shan, R.R.; Du, B. Comparative study on adsorption of basic and acid dyes by hydroxy-aluminum pillared bentonite. *J. Mol. Liq.* **2014**, *199*, 202–207. [[CrossRef](#)]
25. Aguiar, J.E.; Bezerra, B.T.C.; Siqueira, A.C.A.; Barrera, D.; Sapag, K.; Azevedo, D.C.S.; Lucena, S.M.P.; Silva, I.J. Improvement in the Adsorption of Anionic and Cationic Dyes from Aqueous Solutions: A Comparative Study using Aluminium Pillared Clays and Activated Carbon. *Sep. Sci. Technol.* **2014**, *49*, 741–751. [[CrossRef](#)]
26. Trabelsi, H.; Khadhraoui, M.; Hentati, O.; Ksibi, M. Titanium dioxide mediated photo-degradation of methyl orange by ultraviolet light. *Toxicol. Environ. Chem.* **2013**, *95*, 543–558. [[CrossRef](#)]
27. Wu, Q.Y.; Liang, H.Q.; Li, M.; Liu, B.T.; Xu, Z.K. Hierarchically porous carbon membranes derived from PAN and their selective adsorption of organic dyes. *Chin. J. Polym. Sci. (Engl. Ed.)* **2016**, *34*, 23–33. [[CrossRef](#)]
28. Song, S.; Hao, C.; Zhang, X.; Zhang, Q.; Sun, R. Sonocatalytic degradation of methyl orange in aqueous solution using Fe-doped TiO<sub>2</sub> nanoparticles under mechanical agitation. *Open Chem.* **2018**, *16*, 1283–1296. [[CrossRef](#)]
29. Roca Jalil, M.E.; Vieira, R.S.; Azevedo, D.; Baschini, M.; Sapag, K. Improvement in the adsorption of thiabendazole by using aluminum pillared clays. *Appl. Clay Sci.* **2013**, *71*, 55–63. [[CrossRef](#)]
30. Kumararaja, P.; Manjiaiah, K.M.; Datta, S.C.; Sarkar, B. Remediation of metal contaminated soil by aluminium pillared bentonite: Synthesis, characterisation, equilibrium study and plant growth experiment. *Appl. Clay Sci.* **2017**, *137*, 115–122. [[CrossRef](#)]
31. Tan, K.L.; Hameed, B.H. Insight into the adsorption kinetics models for the removal of contaminants from aqueous solutions. *J. Taiwan Inst. Chem. Eng.* **2017**, *74*, 25–48. [[CrossRef](#)]
32. Lagergren, S.K. About the theory of so-called adsorption of soluble substances. *Sven. Vetenskapsakad. Handlingar* **1898**, *24*, 1–39.
33. Ho, Y.S. Review of second-order models for adsorption systems. *J. Hazard. Mater.* **2006**, *136*, 681–689. [[CrossRef](#)] [[PubMed](#)]
34. Ho, Y.; McKay, G. Pseudo-second order model for sorption processes. *Process Biochem.* **1999**, *34*, 451–465. [[CrossRef](#)]
35. Rathnayake, S.I.; Xi, Y.; Frost, R.L.; Ayoko, G.A. Environmental applications of inorganic-organic clays for recalcitrant organic pollutants removal: Bisphenol A. *J. Colloid Interface Sci.* **2016**, *470*, 183–195. [[CrossRef](#)]
36. Langmuir, I. The constitution and fundamental properties of solids and liquids. part I. solids. *J. Am. Chem. Soc.* **1916**, *38*, 2221–2295. [[CrossRef](#)]
37. Langmuir, I. The constitution and fundamental properties of solids and liquids. Part II.—Liquids. *J. Franklin Inst.* **1917**, *184*, 721. [[CrossRef](#)]
38. Freundlich, H.M.F. Over the Adsorption in Solution. *J. Phys. Chem.* **1906**, *57*, 384–470.
39. Ayawei, N.; Ebelegi, A.N.; Wankasi, D. Modelling and Interpretation of Adsorption Isotherms. *J. Chem.* **2017**, *2017*, 1–11. [[CrossRef](#)]
40. Choudhary, B.; Paul, D. Isotherms, kinetics and thermodynamics of hexavalent chromium removal using biochar. *J. Environ. Chem. Eng.* **2018**, *6*, 2335–2343. [[CrossRef](#)]
41. Redlich, O.; Peterson, D.L. A Useful Adsorption Isotherm. *J. Phys. Chem.* **1959**, *63*, 1024. [[CrossRef](#)]
42. Barakan, S.; Aghazadeh, V. Synthesis and characterization of hierarchical porous clay heterostructure from Al, Fe -pillared nano-bentonite using microwave and ultrasonic techniques. *Microporous Mesoporous Mater.* **2019**, *278*, 138–148. [[CrossRef](#)]
43. Zhu, J.; Wen, K.; Wang, Y.; Ma, L.; Su, X.; Zhu, R.; Xi, Y.; He, H. Superior thermal stability of Keggin-Al<sub>30</sub>pillared montmorillonite: A comparative study with Keggin-Al<sub>13</sub>pillared montmorillonite. *Microporous Mesoporous Mater.* **2018**, *265*, 104–111. [[CrossRef](#)]
44. Sartor, L.R.; De Azevedo, A.C.; Andrade, G.R.P. Study of colloidal properties of natural and Al-pillared smectite and removal of copper ions from an aqueous solution. *Environ. Technol.* **2015**, *36*, 786–795. [[CrossRef](#)]
45. Zhu, J.; Wen, K.; Zhang, P.; Wang, Y.; Ma, L.; Xi, Y.; Zhu, R.; Liu, H.; He, H. Keggin-Al<sub>30</sub>pillared montmorillonite. *Microporous Mesoporous Mater.* **2017**, *242*, 256–263. [[CrossRef](#)]
46. Sing, K.S.W.; Everett, D.H.; Haul, R.A.W.; Moscou, L.; Pierotti, R.A.; Rouquerol, J.; Siemieniewska, T. Reporting Physisorption Data for Gas/Solid Systems with Special Reference to the Determination of Surface Area and Porosity. *Pure Appl. Chem.* **1985**, *57*, 603–619. [[CrossRef](#)]
47. Occelli, M.; Bertrand, J.; Gould, S.A.; Dominguez, J. Erratum to: Physicochemical characterization of a Texas montmorillonite pillared with polyoxocations of aluminum. Part I: The microporous structure [Microporous and Mesoporous Materials 34 (2000) 195–206]. *Microporous Mesoporous Mater.* **2000**, *40*, 351. [[CrossRef](#)]
48. Ge, Z.; Li, D.; Pinnavaia, T.J. Preparation of alumina-pillared montmorillonites with high thermal stability, regular microporosity and Lewis/Brønsted acidity. *Microporous Mater.* **1994**, *3*, 165–175. [[CrossRef](#)]
49. Mnasri, S.; Frini-srasra, N. Infrared Physics & Technology Evolution of Brønsted and Lewis acidity of single and mixed pillared bentonite. *Infrared Phys. Technol.* **2013**, *58*, 15–20. [[CrossRef](#)]
50. Wang, K.; Zhang, Y.; Qi, R.; Yang, M.; Deng, R. Effects of activated carbon surface chemistry and pore structure on adsorption of HAAs from water. *Huagong Xuebao/J. Chem. Ind. Eng.* **2006**, *57*, 1659–1663.

51. Huang, R.; Hu, C.; Yang, B.; Zhao, J. Zirconium-immobilized bentonite for the removal of methyl orange (MO) from aqueous solutions. *Desalin. Water Treat.* **2016**, *57*, 10646–10654. [[CrossRef](#)]
52. Bouberka, Z.; Khenifi, A.; Benderdouche, N.; Derriche, Z. Removal of Supranol Yellow 4GL by adsorption onto Cr-intercalated montmorillonite. *J. Hazard. Mater.* **2006**, *133*, 154–161. [[CrossRef](#)] [[PubMed](#)]